NANO LETTERS

pubs.acs.org/NanoLett

Letter

Accessing Highly Oriented Two-Dimensional Perovskite Films via Solvent-Vapor Annealing for Efficient and Stable Solar Cells

Xiaoming Zhao, Tianran Liu, Alan B. Kaplan, Chao Yao, and Yueh-Lin Loo*

Cite This: *Nano Lett.* 2020, 20, 8880−8889

Read Online

ACCESS | Metrics & More | Article Recommendations | Supporting Information

ABSTRACT: Accessing vertical orientation of two-dimensional (2D) perovskite films is key to achieving high-performance solar cells with these materials. Herein, we report on solvent-vapor annealing (SVA) as a general postdeposition strategy to induce strong vertical orientation across broad classes of 2D perovskite films. We do not observe any local compositional drifts that would result in impure phases during SVA. Instead, our experiments point to solvent vapor plasticizing 2D perovskite films and facilitating their surface-induced reorientation and concomitant grain growth, which enhance out-of-plane charge transport. Solar cells with SVA 2D perovskites exhibit superior efficiency and stability compared to their untreated analogs. With a certified efficiency of (18.00 ± 0.30) %, our SVA (BDA)$(Cs_{0.1}FA_{0.9})_4Pb_5I_{16}$ solar cell boasts the highest efficiency among all solar cells with 2D perovskites ($n \leq 5$) reported so far.

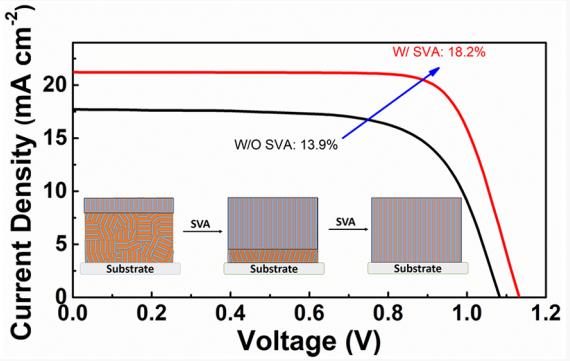

KEYWORDS: *two-dimensional perovskite, crystal orientation, solvent-vapor annealing, solar cells*

The power-conversion efficiencies (PCEs) of three-dimensional (3D) organometal halide perovskite solar cells (PSCs) have sky-rocketed in the past few years with a certified record value that is now over 25%.[1−3] These solar cells, however, suffer from inherent instability when exposed to light, heat, and moisture.[4−6] Recently, layered two-dimensional (2D) perovskites have been developed as the light-harvesting layer for PSCs. These 2D perovskites exhibit substantially improved environmental and structural stability relative to their 3D counterparts.[7−9] PSCs that comprise 2D perovskites, however, have exhibited disappointingly low PCEs by comparison.[9−11] Natively, the alternating organic and inorganic layers in 2D perovskite thin films are preferentially oriented parallel to the substrate when these films are processed from solution, which is believed to hinder out-of-plane charge transport, reducing the performance of PSCs with 2D perovskites compared to those with their 3D counterparts.[12,13]

Accessing 2D perovskite films in which the organic and inorganic layers are vertically oriented should substantively reduce charge-transport resistance and dramatically boost the PCEs of 2D PSCs. Very recently, several deposition approaches[14−18] have been reported to effectively improve the vertical alignment of 2D perovskite films, resulting in PSCs with PCEs as high as 14.1%. A significant drawback to these approaches, however, is that they are only applicable to a narrow class of materials with specific organic spacer chemistries and/or perovskite compositions, and all have focused on MA-comprising Ruddlesden−Popper perovskites. This specificity is not unexpected, given the structural variation in 2D perovskites with organic spacer chemistry and perovskite composition. Among the 2D perovskites that could benefit from vertical orientation, but such preferential orientation has not yet been demonstrated, are those with small interlayer spacings, that is, n = 1 2D perovskites, whose layers exhibit a yet stronger tendency to adopt a face-on orientation with respect to the substrate compared to 2D perovskites with n > 1;[19] Dion-Jacobson (DJ) type 2D perovskites whose diammonium organic spacers leave substantially fewer degrees of freedom for orientation regulation; and those with mixed cations, such as those partially substituted with FA^+ or Cs^+, whose compositional heterogeneity brings added complexity to solidification and reduces phase stability in formed films.[20] A simple, robust and general method to effectively control the crystallization of and layer orientation in 2D perovskites across different chemistries could significantly promote the development of high-quality 2D perovskite films for both PSCs and other thin-film based applications, such as lighting-emitting diodes,[21,22] photodetectors,[23−25] thermoelectrics,[26] spintronics,[27,28] and so forth.

Received: September 29, 2020
Revised: November 1, 2020
Published: November 9, 2020

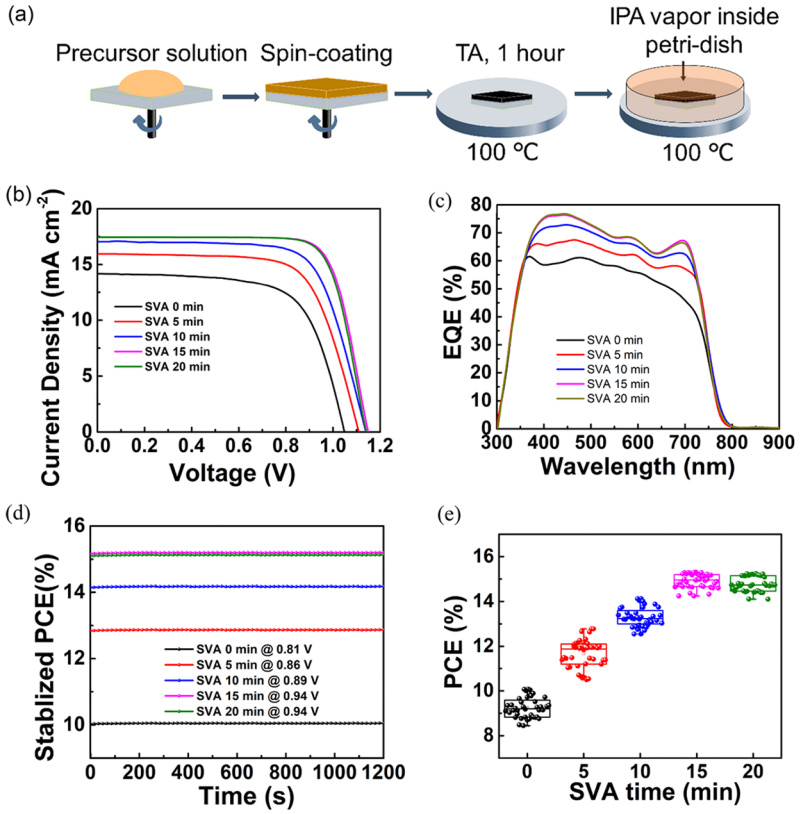

Figure 1. Device performance of solvent-vapor annealed $(PEA)_2MA_4Pb_5I_{16}$ PSCs. (a) Scheme of postdeposition processing of 2D perovskite films. (b) Current−voltage (J−V) characteristics under reverse voltage scan, (c) EQE, (d) stabilized output, and (e) PCE statistics (40 devices per condition) of solar cells based on $(PEA)_2MA_4Pb_5I_{16}$ perovskite films exposed to IPA for varying times.

Table 1. Summary of Champion and Average Photovoltaic Parameters of Solar Cells under Reverse Voltage Scan Based on $(PEA)_2MA_4Pb_5I_{16}$ Treated by SVA with Time[a]

device	J_{SC} (mA cm^{-2})	J_{SC} from EQE (mA cm^{-2})	V_{OC} (V)	FF	PCE (%)
SVA 0 min	14.2 (13.3 ± 0.5)	13.3	1.06 (0.98 ± 0.03)	0.67 (0.64 ± 0.02)	10.1 (9.3 ± 0.5)
SVA 5 min	15.9 (14.8 ± 0.7)	15.0	1.11 (1.03 ± 0.05)	0.72 (0.69 ± 0.03)	12.7 (11.7 ± 0.6)
SVA 10 min	17.0 (16.3 ± 0.5)	16.1	1.15 (1.05 ± 0.05)	0.72 (0.70 ± 0.02)	14.1 (13.3 ± 0.4)
SVA 15 min	17.5 (17.2 ± 0.4)	17.0	1.15 (1.14 ± 0.02)	0.76 (0.75 ± 0.01)	15.3 (14.9 ± 0.3)
SVA 20 min	17.5 (17.1 ± 0.4)	16.9	1.15 (1.14 ± 0.02)	0.76 (0.75 ± 0.01)	15.3 (14.8 ± 0.3)

[a]Average and standard deviation are presented in brackets; these were calculated based on 40 devices at each condition.

Herein, we report isopropanol (IPA) solvent-vapor annealing (SVA) as a general postdeposition strategy to induce preferential vertical orientation and enhanced grain growth across broad classes of 2D perovskites. We first demonstrate this structural rearrangement with a model system of $(PEA)_2(MA)_4Pb_5I_{16}$ and find this preferential vertical orientation to reduce both bulk and surface defects and improve charge transport in and charge transfer at the perovskite and electron transport layer interface. We do not observe compositional drifts that could result in the introduction of low-n and/or 3D phases with SVA. Instead, our experiments point to solvent vapor plasticizing 2D perovskite films and facilitating their surface-induce reorientation and grain growth. PSCs made with IPA-annealed $(PEA)_2(MA)_4Pb_5I_{16}$ exhibit an average PCE of 15.3% up from 10.1%. This postdeposition strategy also induces strong preferential vertical orientation and grain growth in other 2D perovskite systems, including those with smaller interlayer distances, those of DJ-type, and those comprising mixed cations, demonstrating the general effectiveness of this strategy. We report an NREL-certified PCE of (18.00 ± 0.30)% of a PSC comprising SVA-treated $(BDA)(Cs_{0.1}FA_{0.9})_4Pb_5I_{16}$, the highest PCE among PSCs with 2D perovskites ($n \leq 5$) reported so far. In addition, PSCs having SVA-treated 2D perovskites as active layers exhibit superior humidity, thermal, and operational stability.

Figure 1a illustrates the SVA process. Postdeposition SVA decouples structural development from film formation and allows structural rearrangement to take place on plasticization.[29−34] Here, IPA was selected as the solvent of choice because it allows plasticization of perovskite films and enables structural reorganization without inducing dewetting of the films from their substrates. Zheng et al. reported solvent-annealing of $(BA)_2(MA)_3Pb_4I_{13}$ with γ-butyrolactone (GBL) to obtain a solar cell with a PCE that is <5%.[35] Using a solvent in which the perovskite precursors have relatively high solubility (e.g., GBL) can cause complete dewetting of the perovskite films from their substrates. With annealed films

https://dx.doi.org/10.1021/acs.nanolett.0c03914
Nano Lett. 2020, 20, 8880−8889

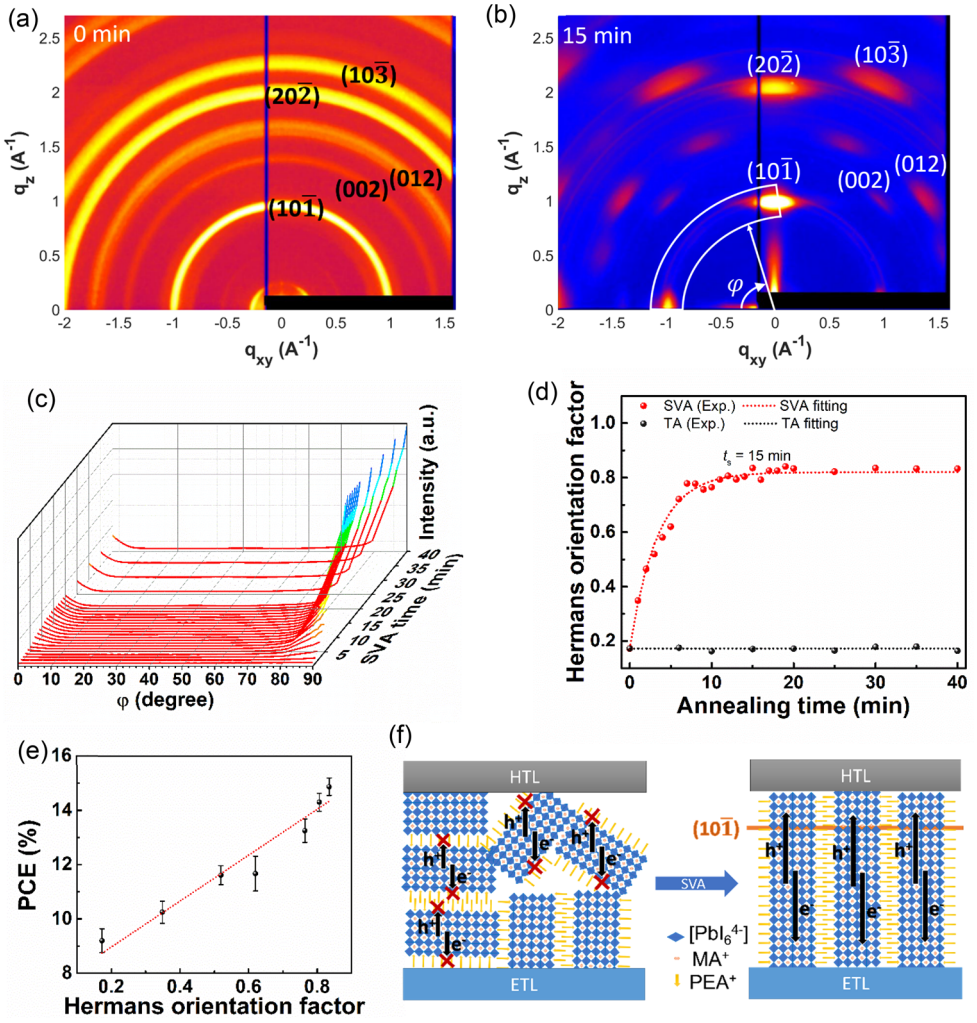

Figure 2. Structural evolution of SVA-perovskite thin films. GIWAXS patterns of $(PEA)_2(MA)_4Pb_5I_{16}$ perovskite films (a) before and (b) after SVA treatment. (c) Azimuthal plots tracking the intensity evolution of the (10$\bar{1}$) reflection of $(PEA)_2(MA)_4Pb_5I_{16}$ as a function of SVA time. (d) Hermans orientation factor tracking the evolution of preferential orientation with SVA and TA. (e) Device PCEs as a function of Hermans orientation factor. (f) Scheme showing the structural evolution from randomly orientated crystallites to vertically orientated grains, induced by SVA treatment.

being rougher and less uniform than pristine films, we are not surprised that solar cells comprising GBL-annealed 2D perovskite films exhibit such moderate PCEs.[35] Figure 1b–e, Figures S1–S2, and Table 1 display the photovoltaic characteristics of PSCs based on $(PEA)_2(MA)_4Pb_5I_{16}$ films that had been exposed to IPA vapor for varying times. With 15 min SVA, all device parameters, including short-circuit current density (J_{SC}), open-circuit voltage (V_{OC}) and fill factor (FF), improve, contributing to a PCE of 15.3%, up from 10.1% for reference PSCs with untreated $(PEA)_2(MA)_4Pb_5I_{16}$.

We briefly entertained the possibility that local compositional drifts in $(PEA)_2(MA)_4Pb_5I_{16}$ could be responsible for the enhanced solar-cell performance we see with SVA. Indeed, numerous reports[10,36−40] have highlighted the presence of lower n-, as well as 3D-phases, in 2D perovskites and the extents of which depend on deposition conditions. To maximize phase purity in our as-cast films, we spin coated from concentrated precursor solutions of 1.25 M in pure DMF.[37,40] Figure S3 contains the photoluminescence (PL) spectra of $(PEA)_2(MA)_4Pb_5I_{16}$ processed at these conditions, and those of $(PEA)_2(MA)_4Pb_5I_{16}$ processed under typical literature conditions, that is, from a mixture of DMF and DMSO, with relevant discussion detailed in Supporting Information. Comparison between these spectra confirms there is no compositional drifts that could result in the introduction of low-n and/or 3D phases with SVA.[37−40] Further, the $(PEA)_2(MA)_4Pb_5I_{16}$ PSCs, independent of whether the active layers were SVA, show the same external quantum efficiency (EQE) band edge that is blue-shifted by 20 nm relative to that of $MAPbI_3$ PSC (Figure S4). These results indicate that 3D impurities, if present, are only present in fractional quantities, and their presence does not contribute to the performance enhancement of our PSCs on SVA.

Figure 2a,b and Figure S5 show the GIWAXS patterns of the corresponding films as a function of SVA time. As reference, the GIWAXS patterns of $(PEA)_2(MA)_4Pb_5I_{16}$ thin films after a second thermal annealing step (TA; an initial mild thermal annealing was applied to all films to drive off residual solvent) are displayed in Figure S6. The GIWAXS patterns in Figure 2a and Figure S6 are comparable, implying that there is no structural change when $(PEA)_2(MA)_4Pb_5I_{16}$ films are further thermally annealed. In particular, the GIWAXS pattern of thermally annealed $(PEA)_2(MA)_4Pb_5I_{16}$ exhibits diffraction rings that correspond to its (10$\bar{1}$), (002), (012), (20$\bar{2}$), and

https://dx.doi.org/10.1021/acs.nanolett.0c03914
Nano Lett. 2020, 20, 8880−8889

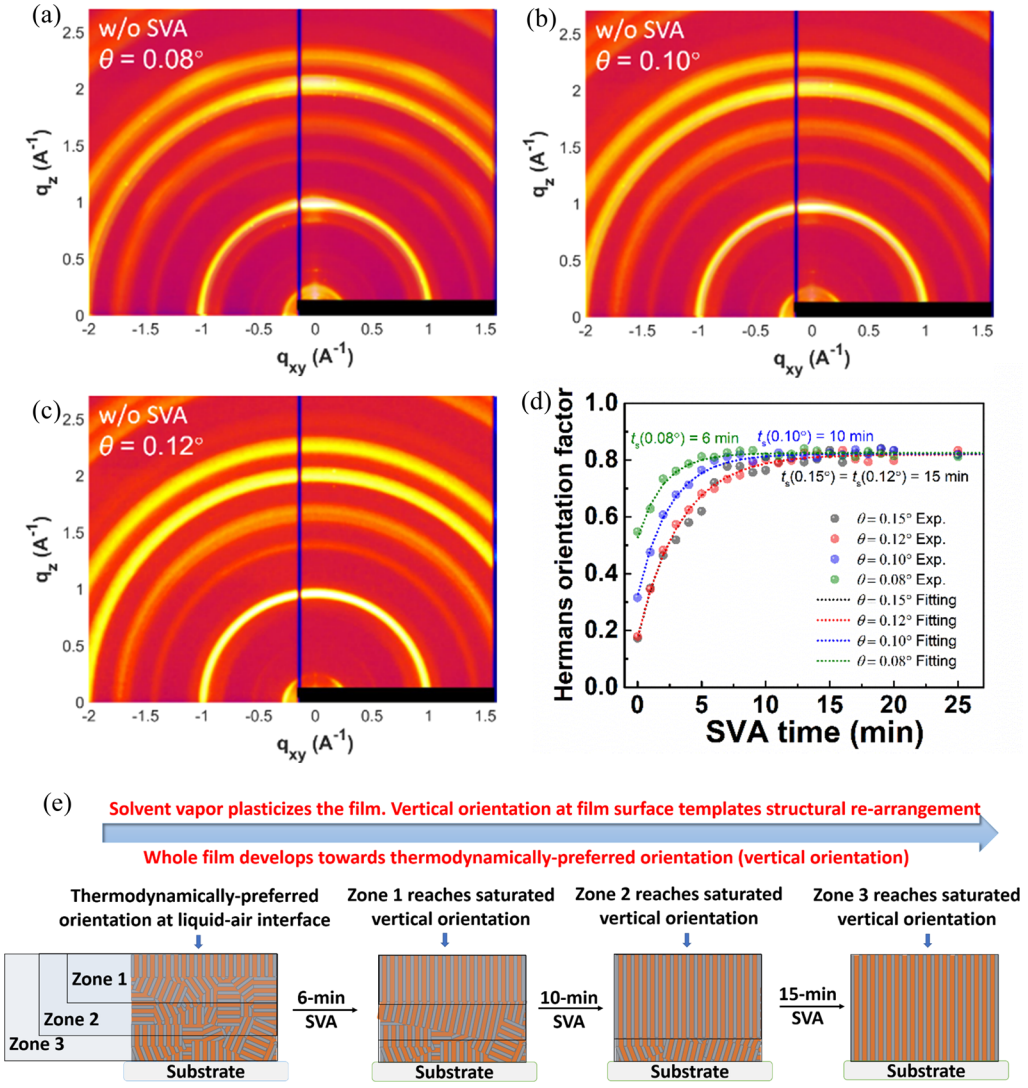

Figure 3. Reorientation mechanism. GIWAXS patterns obtained at X-ray incident angle of (a) 0.08°, (b) 0.10°, and (c) 0.12° for a $(PEA)_2(MA)_4Pb_5I_{16}$ perovskite film before SVA treatment. (d) Hermans orientation factor tracking the evolution of preferential orientation at incident angles of 0.08°, 0.10°, 0.12°, and 0.15° with SVA. (e) Illustration of the reorientation process during SVA.

$(10\bar{3})$ reflections, confirming the preservation of its structure and polycrystallinity. The $(10\bar{1})$ reflection exhibits a slight enhancement in intensity at the meridian (q_z), indicating that, when thermally annealed, $(PEA)_2(MA)_4Pb_5I_{16}$ has a weak preference for its alternating organic and inorganic layers to be vertically oriented (Figure 2a). With SVA, the near-isotropic diffraction rings in the GIWAXS patterns of these films are replaced with discrete Bragg spots (Figure 2b), indicating the development of a distinct preferential orientation. The partial pole figure of the $(10\bar{1})$ reflection of the IPA-annealed $(PEA)_2(MA)_4Pb_5I_{16}$ films plotted in Figure 2c tracks its intensity as a function of azimuthal angle with increasing SVA time. That this intensity distribution narrows and intensifies confirms that SVA enhances the out-of-plane orientation. To quantify the extent of preferential orientation, we calculated the Hermans orientation factor ($H(10\bar{1})$) of the $(10\bar{1})$ reflection according to eq 1 and 2[41]

$$\langle \cos^2\varphi \rangle = \frac{\int_0^{\pi} I(\varphi)\cos^2\varphi \sin\varphi \, d\varphi}{\int_0^{\pi} I(\varphi)\sin\varphi \, d\varphi} \quad (1)$$

$$H(10\bar{1}) = \frac{3\langle \cos^2\varphi \rangle - 1}{2} \quad (2)$$

where φ is the azimuthal angle from 0° to 90° and $I(\varphi)$ is the angle-dependent scattering intensity. In this context, $H(10\bar{1})$ = 0 corresponds to randomly oriented crystallites; $H(10\bar{1})$ = 1 corresponds to a film whose alternating layers adopt a perfectly vertical orientation, and $H(10\bar{1})$ = −0.5 indicates a perfectly horizontal orientation. Tracking $H(10\bar{1})$ as a function of solvent-vapor annealing time (Figure 2d) reveals an increase from 0.17 to 0.83, with a reorientation saturation time (t_S) of 15 min, when $(PEA)_2(MA)_4Pb_5I_{16}$ is annealed in a saturated IPA atmosphere at 100 °C. The PCEs of PSCs comprising these films show strong positive correlation with the evolution of the Hermans orientation factor, as displayed in Figure 2e. This correlation strongly suggests that the enhanced preferential orientation induced by SVA treatment to first order accounts for the dramatically enhanced PCE of PSCs comprising these films. As shown in Figure 2f, vertically orienting the alternating organic and inorganic layers in $(PEA)_2(MA)_4Pb_5I_{16}$ minimizes the resistance to out-of-plane charge transport presented by the insulating organic spacers in

https://dx.doi.org/10.1021/acs.nanolett.0c03914
Nano Lett. 2020, 20, 8880−8889

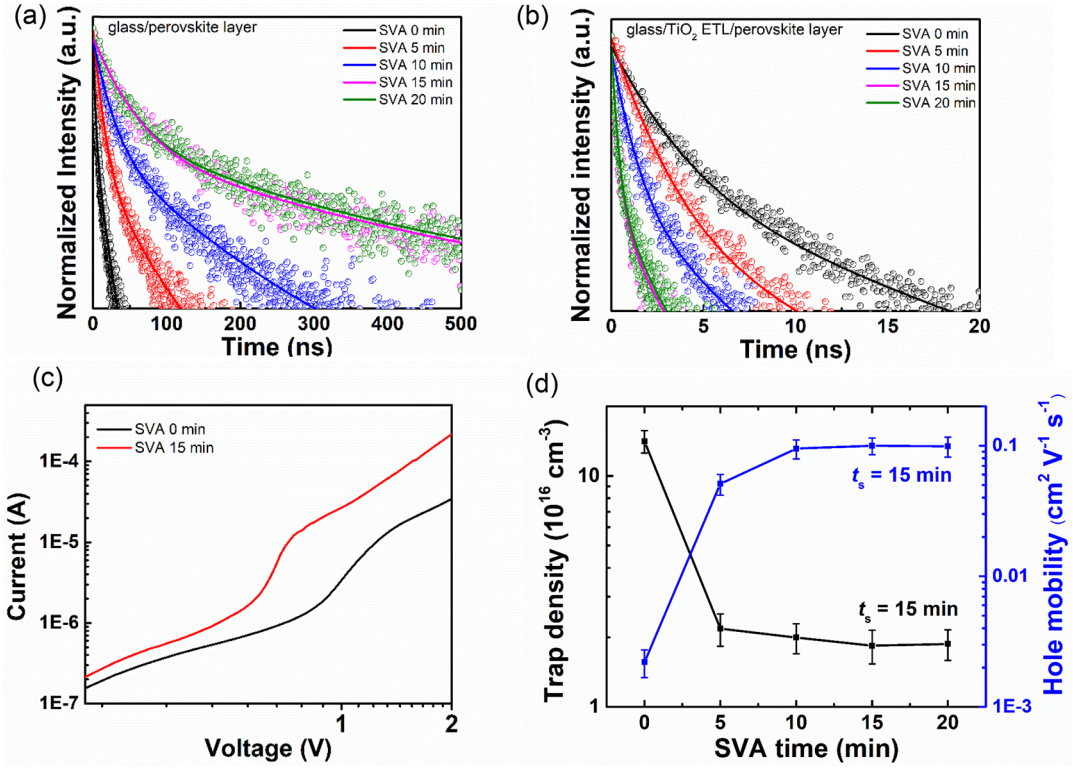

Figure 4. Charge extraction and transport properties of SVA-treated perovskite thin films. Time-resolved PL spectra of $(PEA)_2MA_4Pb_5I_{16}$ thin films deposited (a) on quartz glass and (b) on TiO_2-coated quartz glass treated by SVA with time. (c) Dark current density−voltage (J−V) characteristics extracted from the PV-SCLC measurement of representative hole-only devices based on a $(PEA)_2MA_4Pb_5I_{16}$ thin film treated by SVA for 0 and 15 min, and (d) calculated trap density and hole mobility extracted from such devices with their active layers treated by SVA for varying times (average values were obtained based on five devices at each condition).

2D perovskite thin films and leads to higher quality electrically active thin films with lower defect density and higher charge carrier mobility.

GIWAXS measurements on $(PEA)_2(MA)_4Pb_5I_{16}$ with SVA exposure as a function of X-ray incident angle yielded insight on the mechanism of reorientation. As we increase the incident angle during these measurements, we can probe deeper into the films. As an example, we show the GIWAXS patterns that were obtained at three different X-ray incident angles of 0.08°, 0.10°, and 0.12° of an as-cast $(PEA)_2(MA)_4Pb_5I_{16}$ film in Figure 3a−c. For reference, the critical angle of the film is 0.11°. The $H(10\bar{1})$ extracted from these GIWAXS patterns are 0.55, 0.42, and 0.18, respectively. This analysis reveals a strong surface effect; the surface of the $(PEA)_2(MA)_4Pb_5I_{16}$ is substantially more vertically oriented than the bulk. Integrating across the depth of the film yields an orientation factor that is substantially less than that of the surface alone. This observation is consistent with several reports that preferential vertical orientation in 2D perovskites originates from the liquid−air interface.[18,42−45] We plotted the $H(10\bar{1})$ tracking the structural evolution of $(PEA)_2(MA)_4Pb_5I_{16}$ with SVA at these different incident angles in Figure 3d. That the evolution of $H(10\bar{1})$ with SVA obtained at 0.12° and 0.15° are almost identical confirms that we are probing the structural evolution of the bulk of $(PEA)_2(MA)_4Pb_5I_{16}$ at these two incident angles. Tracking the $H(10\bar{1})$ with SVA at shallower incident angles reveals that reorientation is fastest at the surface of film; the reorientation time constant increases progressively with increasing incident angle. Collectively, we surmise that IPA vapor plasticizes $(PEA)_2(MA)_4Pb_5I_{16}$ and provides sufficient mobility for the surface to reorient and adopt its thermodynamically more favored orientation given surface energetics. We have schematized this process in Figure 3e in which the surface portion of the film (Zone 1) reorients first; this reorientation presumably templates subsequent reorientation in Zones 2 then 3. The PL spectra acquired at different time points of SVA of $(PEA)_2(MA)_4Pb_5I_{16}$ from the glass side and from the surface side are shown in Figure S7. That the emission evolution when excitation from the film side (probing near surface) saturates before the emission evolution when excitation is from the glass side (probing the bulk) is further evidence of surface-induce reorientation of $(PEA)_2(MA)_4Pb_5I_{16}$ when it is exposed to SVA. The peak luminescence of $(PEA)_2(MA)_4Pb_5I_{16}$ after a 20 min SVA shows a 20 nm red shift compared to that of untreated $(PEA)_2(MA)_4Pb_5I_{16}$. Because we have ruled out compositional drifts that can result in the incorporation of 3D phases, we believe this red shift in PL emission stems from an increase in the grain size of $(PEA)_2(MA)_4Pb_5I_{16}$ with SVA.[46,47] Figure S8 shows AFM micrographs acquired on one such perovskite film before and after SVA. Consistent with the quantitative red shifts in PL emission that have been reported in the literature,[46,47] we observe the grain size to increase from about 100 nm to about 2 μm after SVA.

To understand the impact of SVA-induced reorientation on charge-carrier dynamics, we carried out time-resolved photoluminescence (TRPL) spectroscopy on $(PEA)_2(MA)_4Pb_5I_{16}$ deposited on bare glass and on TiO_2-coated glass (Figure 4a,b). We fitted the TRPL curves with a biexponential decay function (eq 3)[48]

https://dx.doi.org/10.1021/acs.nanolett.0c03914
Nano Lett. 2020, 20, 8880−8889

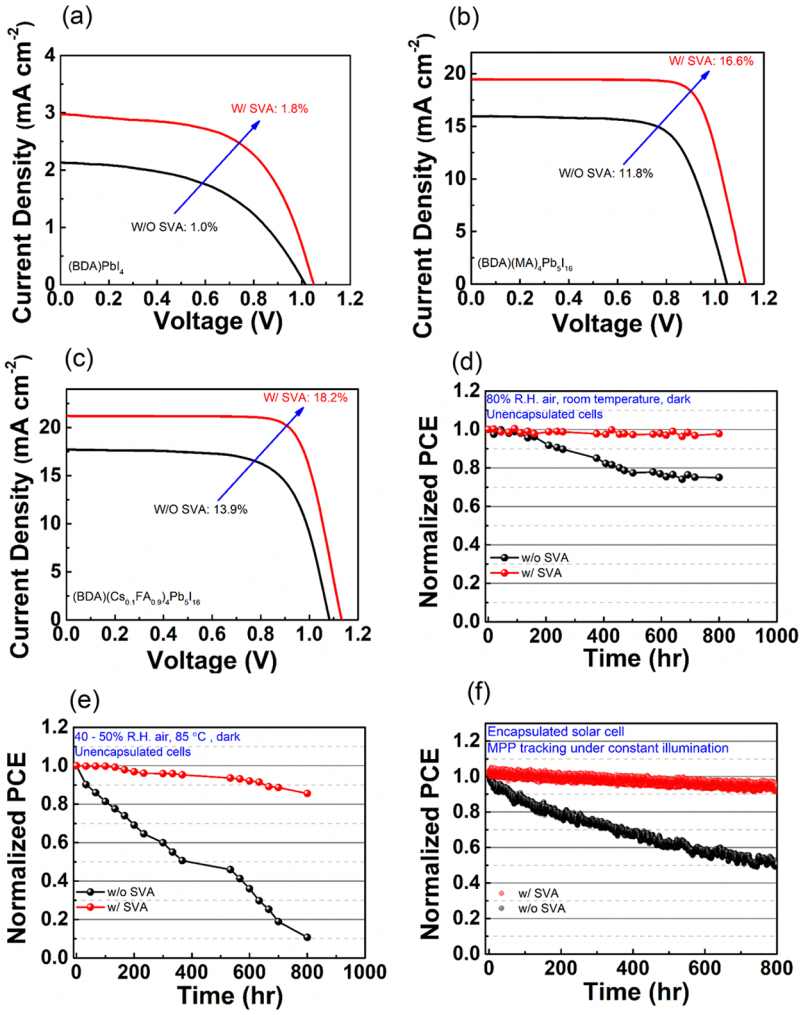

Figure 5. Generality of SVA strategy and solar cell stability. Current density−voltage (J−V) characteristics of PSCs under reverse voltage scan based on (a) $(BDA)PbI_4$, (b) $(BDA)(MA)_4Pb_5I_{16}$, and (c) $(BDA)(Cs_{0.1}FA_{0.9})_4Pb_5I_{16}$ perovskite thin films with and without SVA treatment. (d) Normalized PCE as a function of storage time of unencapsulated solar cells based on $(BDA)(Cs_{0.1}FA_{0.9})_4Pb_5I_{16}$ thin films with and without SVA. The aging condition is ∼80% R.H. air and ∼20 °C in the dark. (e) Normalized PCE as a function of storage time of unencapsulated solar cells based on $(BDA)(Cs_{0.1}FA_{0.9})_4Pb_5I_{16}$ thin films with and without SVA. The aging condition is 40−50% R.H. air and ∼85 °C in the dark. (f) Normalized PCE as a function of aging time of encapsulated solar cells under continuous illumination based on $(BDA)(Cs_{0.1}FA_{0.9})_4Pb_5I_{16}$ thin films with and without SVA. The cell configuration is FTO/c-TiO_2/m-TiO_2/$(BDA)(Cs_{0.1}FA_{0.9})_4Pb_5I_{16}$ with or without SVA treatment/dopant-free ST1/Cr/Au.

$$f(t) = A_1 \exp\left(-\frac{t}{\tau_1}\right) + A_1 \exp\left(-\frac{t}{\tau_1}\right) + B \quad (3)$$

where τ_1 and τ_2 are the fast and slow decay time constants, respectively, A_1 and A_2 are their corresponding decay amplitudes, and B is a constant. The extracted decay times are summarized in Tables S1 and S2 with τ_1 representing the time for quenching via trap states or interfacial charge transfer, and τ_2 representing the carrier lifetime, which in turn provides an inverse quantification for the extent of carrier recombination in the bulk.[49,50] We found τ_2 to increase from 20 to 395 ns after 15 min SVA; this substantively increased carrier lifetime implies successful suppression of nonradiative recombination in vertically oriented $(PEA)_2(MA)_4Pb_5I_{16}$ with increased grain size.[49] Furthermore, we tracked the TRPL decay of $(PEA)_2(MA)_4Pb_5I_{16}$ films on substrates coated with TiO_2, the electron transport layer (ETL) of choice in our PSCs. Both τ_1 and τ_2 of untreated $(PEA)_2(MA)_4Pb_5I_{16}$ on TiO_2-coated substrates are comparable to those on films deposited on bare glass; the introduction of ETL does not appear to improve charge transfer from as-deposited $(PEA)_2(MA)_4Pb_5I_{16}$. Compared to the decay time of such an untreated film (3 ns), τ_1 of SVA-treated $(PEA)_2(MA)_4Pb_5I_{16}$ decreases to 0.3 ns after a 15 min SVA treatment. In the presence of the ETL, we take a shorter τ_1 to mean more efficient electron transfer and carrier extraction at the interface between $(PEA)_2(MA)_4Pb_5I_{16}$ and TiO_2, which we surmise to stem from reduced defects at the electron-selective interface in PSCs having SVA-treated $(PEA)_2(MA)_4Pb_5I_{16}$.[51,52] We further studied the impact of SVA-induced reorientation on charge-carrier mobility and trap density of 2D perovskite thin films. Because 2D perovskites are reported to be intrinsic semiconductors ($\mu_h \approx \mu_e$, where μ_h and μ_e are hole and electron mobilities, respectively),[53,54] we fabricated hole-only devices, performed I−V measurements and calculated the hole mobility and trap density according to a recently reported pulsed-voltage space-charge limited current procedure (PV-SCLC).[55] We found the out-of-plane mobility to increase by almost 2 orders of magnitude from (0.0022 ±

https://dx.doi.org/10.1021/acs.nanolett.0c03914
Nano Lett. 2020, 20, 8880−8889

Table 2. Summary of Champion and Average Photovoltaic Parameters of Solar Cells under Reverse Voltage Scan Based on $(BDA)PbI_4$, $(BDA)(MA)_4Pb_5I_{16}$ and $(BDA)(Cs_{0.1}FA_{0.9})_4Pb_5I_{16}$ with and without SVA[a]

device	J_{SC} (mA cm^{-2})	J_{SC} from EQE (mA cm^{-2})	V_{OC} (V)	FF	PCE (%)
$(BDA)PbI_4$ w/o SVA	2.1 (1.7 ± 0.3)	2.0	1.01 (0.95 ± 0.06)	0.49 (0.43 ± 0.10)	1.0 (0.6 ± 0.4)
$(BDA)PbI_4$ w/SVA	2.9 (2.8 ± 0.3)	2.7	1.04 (1.00 ± 0.05)	0.61 (0.55 ± 0.10)	1.8 (1.5 ± 0.4)
$(BDA)(MA)_4Pb_5I_{16}$ w/o SVA	15.9 (14.7 ± 0.4)	15.1	1.04 (0.99 ± 0.04)	0.71 (0.68 ± 0.03)	11.8 (10.6 ± 0.4)
$(BDA)(MA)_4Pb_5I_{16}$ w/SVA	19.5 (18.4 ± 0.2)	18.7	1.13 (1.11 ± 0.03)	0.75 (0.74 ± 0.02)	16.5 (15.4 ± 0.3)
$(BDA)(Cs_{0.1}FA_{0.9})_4Pb_5I_{16}$ w/o SVA	18.5 (17.9 ± 0.5)	18.1	1.04 (0.99 ± 0.06)	0.72 (0.71 ± 0.02)	13.9 (12.3 ± 0.4)
$(BDA)(Cs_{0.1}FA_{0.9})_4Pb_5I_{16}$ w/SVA	21.2 (20.9 ± 0.3)	20.9	1.13 (1.10 ± 0.02)	0.76 (0.75 ± 0.02)	18.2 (17.9 ± 0.4)

[a]Average and standard deviation are presented in brackets; these parameters were calculated based on 40 devices at each condition.

0.0005) to (0.10 ± 0.02) cm^2 V^{-1} s^{-1}, and the trap density to decrease from (14.1 ± 1.6) × 10^{16} cm^{-3} to (1.8 ± 0.3) × 10^{16} cm^{-3} after a simple 15 min SVA treatment (Figure 4c,d). Consistent with the structural evolution of the perovskite films and the performance enhancements of PSCs comprising them, the evolution of these charge-transport parameters also saturate after 15 min of SVA, implying that we can trace these improvements to SVA-induced reorientation and grain growth of $(PEA)_2(MA)_4Pb_5I_{16}$ active layers.

To explore its generality, we extended our SVA strategy to other 2D perovskite systems including an n = 1 2D perovskite, namely $(BDA)PbI_4$, which comprises a thinner quantum well compared to our model system of $(PEA)_2(MA)_4Pb_5I_{16}$, a Dion-Jacobson 2D perovskite $(BDA)(MA)_4Pb_5I_{16}$, and 2D perovskites with triple cations $(BDA)(Cs_{0.1}FA_{0.9})_4Pb_5I_{16}$. Not unlike the vertical orientation induced in $(PEA)_2(MA)_4Pb_5I_{16}$, we found this SVA treatment to effectively tune the orientation of and increase the grain size in these perovskite thin films (Figures S9–S11) which dramatically improves the performance of PSCs comprising other types of 2D perovskites (Figure 5a,b, Figures S12–S15 and Table 2). In particular, the PSC with SVA-treated $(BDA)(Cs_{0.1}FA_{0.9})_4Pb_5I_{16}$ exhibits an NREL-certified PCE of (18.00 ± 0.30)% (Figure S16), which is among the highest PCEs reported for PSCs comprising $n \leq 5$ 2D perovskites.

We compared the phase purity of our $(BDA)(MA)_4Pb_5I_{16}$ and $(BDA)(Cs_{0.1}FA_{0.9})_4Pb_5I_{16}$ films before and after SVA by comparing their UV–vis absorption, PL, and EQE spectra with their associated 3D counterparts of $MAPbI_3$ and $Cs_{0.1}FA_{0.9}PbI_3$ (relevant discussion detailed in Figures S12–S18). Consistently, we do not observe compositional drifts that could result in the introduction of low-n and/or 3D phases with SVA. As a final and most unambiguous control experiment, we subjected $(BDA)PbI_4$, an n = 1 2D perovskite, to the same scrutiny. On SVA of $(BDA)PbI_4$ film, we observe a similar enhancement in its solar-cell performance. In the absence of the possibility to adopt a different phase, we are left to believe the critical role SVA plays in inducing preferential vertical orientation and increasing grain size, thereby enhancing solar-cell performance of 2D perovskites.

Two-dimensional PSCs with active layers adopting a face-on orientation have generally been reported to exhibit superior stability compared to their 3D counterparts, likely because the perovskite layers are surface-terminated with hydrophobic organics.[56] It is unclear, however, whether this stability is preserved when the 2D perovskite active layers adopt a vertical orientation. To investigate, we performed long-term stability tests of PSCs based on untreated and SVA-treated $(BDA)(Cs_{0.1}FA_{0.9})_4Pb_5I_{16}$. For these measurements, we replaced the Li-doped Spiro-OMeTAD and Au contact with a dopant-free hole-transport material, ST1,[57] and used Cr (10 nm)/Au (80 nm) as the electrode.[58] The latter contact combination is more stable and allowed us to assess the stability of our PSCs at more aggressive conditions of 80% relative humidity, at 85 °C, and under constant illumination. For completeness, we have included the J–V characteristics, PV parameters, and stabilities of PSCs with the two different types of contacts in Figure S19–21 and Table S3. As shown in Figure 5d, the reference PSC with untreated $(BDA)(Cs_{0.1}FA_{0.9})_4Pb_5I_{16}$ under 80% humidity lost over 20% of its original PCE after 800 h, while our champion unencapsulated PSC based on SVA-treated $(BDA)(Cs_{0.1}FA_{0.9})_4Pb_5I_{16}$ exhibited negligible degradation, retaining almost 100% of the original PCE after 800 h. We believe the increase in grain size, and thus decrease in grain boundary density, to be responsible for the enhancement in stability of PSCs comprising SVA-perovskite films.[59] As shown in Figure 5e, the reference PSC with untreated $(BDA)(Cs_{0.1}FA_{0.9})_4Pb_5I_{16}$ stored at 85 °C lost 20% of its original PCE after 100 h and degraded 90% after 800 h. In comparison, our champion unencapsulated PSC based on SVA-treated $(BDA)(Cs_{0.1}FA_{0.9})_4Pb_5I_{16}$ exhibited much slower degradation, retaining more than 80% PCE after 800 h. We then tracked the maximum power point (MPP) to quantify the operational stability of encapsulated devices based on untreated and SVA-treated $(BDA)(Cs_{0.1}FA_{0.9})_4Pb_5I_{16}$ films under continuous illumination (powder density ≈ 1.1 sun, Figure S22) at ambient conditions (about 30 °C, 35% R.H.). As shown in Figure 5f, our champion SVA-treated $(BDA)(Cs_{0.1}FA_{0.9})_4Pb_5I_{16}$ PSC retained over 90% of its initial PCE after 800 h and exhibited negligible "burn-in" degradation, while the PSC with untreated $(BDA)(Cs_{0.1}FA_{0.9})_4Pb_5I_{16}$ lost 50% of its initial PCE after the same exposure and showed "burn-in" degradation in the first 20 h of the experiment. Since this burn-in has been attributed to illumination-induced ion migration in the literature,[60,61] we believe the improved operational stability of encapsulated SVA devices to stem from suppressed ion migration in highly oriented and large-grain $(BDA)(Cs_{0.1}FA_{0.9})_4Pb_5I_{16}$.[62−64] While this hypothesis is still being tested, our results indicate this SVA treatment not only dramatically improves solar-cell performance but also significantly enhances their environmental and operational stability.

In conclusion, we have demonstrated a simple and generally effective postdeposition strategy, being solvent vapor annealing, to access strong vertical orientation and large grain size with a wide range of 2D perovskites. The resulting perovskite films exhibit lower defect densities and higher mobilities than their untreated counterparts, which contribute to high power-conversion efficiencies and stability in PSCs that comprise them. This strategy can be extended to any 2D perovskite-related applications that require low-defect and high-mobility polycrystalline films as it provides exquisite control over the structural development of perovskite active layers; combining

https://dx.doi.org/10.1021/acs.nanolett.0c03914
Nano Lett. 2020, 20, 8880−8889

this approach with custom-designed functional organic spacers, for example, those that readily transport charge, should further boost solar cell efficiencies.

■ ASSOCIATED CONTENT

Supporting Information

The Supporting Information is available free of charge at https://pubs.acs.org/doi/10.1021/acs.nanolett.0c03914.

Experimental methods, additional figures, tables and discussions (PDF)

■ AUTHOR INFORMATION

Corresponding Author

Yueh-Lin Loo − *Department of Chemical and Biological Engineering and Andlinger Center for Energy and the Environment, Princeton University, Princeton, New Jersey 08544, United States;* orcid.org/0000-0002-4284-0847; Email: lloo@princeton.edu

Authors

Xiaoming Zhao − *Department of Chemical and Biological Engineering, Princeton University, Princeton, New Jersey 08544, United States;* orcid.org/0000-0002-1231-3931

Tianran Liu − *Department of Electrical Engineering, Princeton University, Princeton, New Jersey 08544, United States*

Alan B. Kaplan − *Department of Electrical Engineering, Princeton University, Princeton, New Jersey 08544, United States*

Chao Yao − *Department of Chemical and Biological Engineering, Princeton University, Princeton, New Jersey 08544, United States*

Complete contact information is available at: https://pubs.acs.org/10.1021/acs.nanolett.0c03914

Notes

The authors declare no competing financial interest.

■ ACKNOWLEDGMENTS

The authors thank Dr. E. Tsai and Dr. R. Li for their help with X-ray scattering measurements, which were conducted at the Center for Functional Nanomaterials (CFN) and the Complex Materials Scattering (CMS) beamline of the National Synchrotron Light Source II (NSLS-II), which both are U.S. DOE Office of Science Facilities, at Brookhaven National Laboratory under Contract No. DE-SC0012704. The authors acknowledge the use of Princeton's Imaging and Analysis Center, which is partially supported by the Princeton Center for Complex Materials, a National Science Foundation (NSF)-MRSEC program (DMR-1420541). Y.-L. Loo acknowledges support from the National Science Foundation under Grants DMR-1420541, CMMI-1824674, and the U.S. Department of Energy's Office of Energy Efficiency and Renewable Energy (EERE) under Solar Energy Technologies Office (SETO) Agreement Number DE-EE0008560.

■ REFERENCES

(1) Kojima, A.; Teshima, K.; Shirai, Y.; Miyasaka, T. Organometal Halide Perovskites as Visible-Light Sensitizers for Photovoltaic Cells. *J. Am. Chem. Soc.* **2009**, *131* (17), 6050−6051.

(2) National Renewable Energy Laboratory. *Best research-cellefficiencies chart*; 2020 https://www.nrel.gov/pv/assets/pdfs/best-research-cell-efficiencies.20200925.pdf (accessed October 26, 2020).

(3) Turren-Cruz, S. H.; Hagfeldt, A.; Saliba, M. Methylammonium-Free, High-Performance, and Stable Perovskite Solar Cells on a Planar Architecture. *Science (Washington, DC, U. S.)* **2018**, *362* (6413), 449−453.

(4) Tiep, N. H.; Ku, Z.; Fan, H. J. Recent Advances in Improving Stability of PSCs. *Adv. Energy Mater.* **2016**, *6* (3), 1501420.

(5) Zhao, X.; Yao, C.; Gu, K.; Liu, T.; Xia, Y.; Loo, Y.-L. A Hole-Transport Material That Also Passivates Perovskite Surface Defects for Solar Cells with Improved Efficiency and Stability. *Energy Environ. Sci.* **2020**, DOI: 10.1039/D0EE01655A.

(6) Zhao, X.; Yao, C.; Liu, T.; Hamill, J. C.; Ngongang Ndjawa, G. O.; Cheng, G.; Yao, N.; Meng, H.; Loo, Y.-L. Extending the Photovoltaic Response of Perovskite Solar Cells into the Near-Infrared with a Narrow-Bandgap Organic Semiconductor. *Adv. Mater.* **2019**, *31* (49), 1904494.

(7) Stoumpos, C. C.; Cao, D. H.; Clark, D. J.; Young, J.; Rondinelli, J. M.; Jang, J. I.; Hupp, J. T.; Kanatzidis, M. G. Ruddlesden-Popper Hybrid Lead Iodide Perovskite 2D Homologous Semiconductors. *Chem. Mater.* **2016**, *28* (8), 2852−2867.

(8) Cao, D. H.; Stoumpos, C. C.; Farha, O. K.; Hupp, J. T.; Kanatzidis, M. G. 2D Homologous Perovskites as Light-Absorbing Materials for Solar Cell Applications. *J. Am. Chem. Soc.* **2015**, *137* (24), 7843−7850.

(9) Smith, I. C.; Hoke, E. T.; Solis-Ibarra, D.; McGehee, M. D.; Karunadasa, H. I. A Layered Hybrid Perovskite Solar-Cell Absorber with Enhanced Moisture Stability. *Angew. Chem., Int. Ed.* **2014**, *53* (42), 11232−11235.

(10) Koh, T. M.; Shanmugam, V.; Schlipf, J.; Oesinghaus, L.; Müller-Buschbaum, P.; Ramakrishnan, N.; Swamy, V.; Mathews, N.; Boix, P. P.; Mhaisalkar, S. G. Nanostructuring Mixed-Dimensional Perovskites: A Route Toward Tunable, Efficient Photovoltaics. *Adv. Mater.* **2016**, *28* (19), 3653−3661.

(11) Tsai, H.; Asadpour, R.; Blancon, J. C.; Stoumpos, C. C.; Even, J.; Ajayan, P. M.; Kanatzidis, M. G.; Alam, M. A.; Mohite, A. D.; Nie, W. Design Principles for Electronic Charge Transport in Solution-Processed Vertically Stacked 2D Perovskite Quantum Wells. *Nat. Commun.* **2018**, *9* (1), 2130.

(12) Qing, J.; Liu, X. K.; Li, M.; Liu, F.; Yuan, Z.; Tiukalova, E.; Yan, Z.; Duchamp, M.; Chen, S.; Wang, Y.; et al. Aligned and Graded Type-II Ruddlesden−Popper Perovskite Films for Efficient Solar Cells. *Adv. Energy Mater.* **2018**, *8* (21), 1800185.

(13) Zhang, X.; Wu, G.; Fu, W.; Qin, M.; Yang, W.; Yan, J.; Zhang, Z.; Lu, X.; Chen, H. Orientation Regulation of Phenylethylammonium Cation Based 2D Perovskite Solar Cell with Efficiency Higher Than 11%. *Adv. Energy Mater.* **2018**, *8* (14), 1702498.

(14) Tsai, H.; Nie, W.; Blancon, J. C.; Stoumpos, C. C.; Asadpour, R.; Harutyunyan, B.; Neukirch, A. J.; Verduzco, R.; Crochet, J. J.; Tretiak, S.; et al. High-Efficiency Two-Dimensional Ruddlesden-Popper Perovskite Solar Cells. *Nature* **2016**, *536* (7616), 312−317.

(15) Zhang, X.; Ren, X.; Liu, B.; Munir, R.; Zhu, X.; Yang, D.; Li, J.; Liu, Y.; Smilgies, D. M.; Li, R.; et al. Stable High Efficiency Two-Dimensional Perovskite Solar Cells via Cesium Doping. *Energy Environ. Sci.* **2017**, *10* (10), 2095−2102.

(16) Zhang, X.; Wu, G.; Yang, S.; Fu, W.; Zhang, Z.; Chen, C.; Liu, W.; Yan, J.; Yang, W.; Chen, H. Vertically Oriented 2D Layered Perovskite Solar Cells with Enhanced Efficiency and Good Stability. *Small* **2017**, *13* (33), 1700611.

(17) Fu, W.; Wang, J.; Zuo, L.; Gao, K.; Liu, F.; Ginger, D. S.; Jen, A. K. Y. Two-Dimensional Perovskite Solar Cells with 14.1% Power Conversion Efficiency and 0.68% External Radiative Efficiency. *ACS Energy Lett.* **2018**, *3* (9), 2086−2093.

(18) Chen, A. Z.; Shiu, M.; Ma, J. H.; Alpert, M. R.; Zhang, D.; Foley, B. J.; Smilgies, D. M.; Lee, S. H.; Choi, J. J. Origin of Vertical Orientation in Two-Dimensional Metal Halide Perovskites and Its Effect on Photovoltaic Performance. *Nat. Commun.* **2018**, *9* (1), 1336.

(19) Yao, K.; Wang, X.; Xu, Y. X.; Li, F.; Zhou, L. Multilayered Perovskite Materials Based on Polymeric-Ammonium Cations for Stable Large-Area Solar Cell. *Chem. Mater.* **2016**, *28* (9), 3131−3138.

(20) Seok, S. Il; Grätzel, M.; Park, N. Methodologies toward Highly Efficient Perovskite Solar Cells. *Small* **2018**, *14* (20), 1704177.
(21) Yuan, M.; Quan, L. N.; Comin, R.; Walters, G.; Sabatini, R.; Voznyy, O.; Hoogland, S.; Zhao, Y.; Beauregard, E. M.; Kanjanaboos, P.; et al. Perovskite Energy Funnels for Efficient Light-Emitting Diodes. *Nat. Nanotechnol.* **2016**, *11* (10), 872−877.
(22) Wang, N.; Cheng, L.; Ge, R.; Zhang, S.; Miao, Y.; Zou, W.; Yi, C.; Sun, Y.; Cao, Y.; Yang, R.; et al. Perovskite Light-Emitting Diodes Based on Solution-Processed Self-Organized Multiple Quantum Wells. *Nat. Photonics* **2016**, *10* (11), 699−704.
(23) Yu, D.; Cao, F.; Shen, Y.; Liu, X.; Zhu, Y.; Zeng, H. Dimensionality and Interface Engineering of 2D Homologous Perovskites for Boosted Charge-Carrier Transport and Photodetection Performances. *J. Phys. Chem. Lett.* **2017**, *8* (12), 2565−2572.
(24) Wang, J.; Li, J.; Lan, S.; Fang, C.; Shen, H.; Xiong, Q.; Li, D. Controllable Growth of Centimeter-Sized 2D Perovskite Heterostructures for Highly Narrow Dual-Band Photodetectors. *ACS Nano* **2019**, *13* (5), 5473−5484.
(25) Zhao, X.; Liu, T.; Shi, W.; Hou, X.; Dennis, T. J. S. Capillary-Written Single-Crystalline All-Inorganic Perovskite Microribbon Arrays for Highly-Sensitive and Thermal-Stable Photodetectors. *Nanoscale* **2019**, *11* (5), 2453−2459.
(26) Liu, T.; Zhao, X.; Li, J.; Liu, Z.; Liscio, F.; Milita, S.; Schroeder, B. C.; Fenwick, O. Enhanced Control of Self-Doping in Halide Perovskites for Improved Thermoelectric Performance. *Nat. Commun.* **2019**, *10* (1), 5750.
(27) Zhai, Y.; Baniya, S.; Zhang, C.; Li, J.; Haney, P.; Sheng, C. X.; Ehrenfreund, E.; Vardeny, Z. V. Giant Rashba Splitting in 2D Organic-Inorganic Halide Perovskites Measured by Transient Spectroscopies. *Sci. Adv.* **2017**, *3* (7), No. e1700704.
(28) Long, G.; Jiang, C.; Sabatini, R.; Yang, Z.; Wei, M.; Quan, L. N.; Liang, Q.; Rasmita, A.; Askerka, M.; Walters, G.; et al. Spin Control in Reduced-Dimensional Chiral Perovskites. *Nat. Photonics* **2018**, *12*, 528−533.
(29) Dickey, K. C.; Anthony, J. E.; Loo, Y.-L. Improving Organic Thin-Film Transistor Performance through Solvent-Vapor Annealing of Solution-Processable Triethylsilylethynyl Anthradithiophene. *Adv. Mater.* **2006**, *18* (13), 1721−1726.
(30) Hiszpanski, A. M.; Baur, R. M.; Kim, B.; Tremblay, N. J.; Nuckolls, C.; Woll, A. R.; Loo, Y. L. Tuning Polymorphism and Orientation in Organic Semiconductor Thin Films via Post-Deposition Processing. *J. Am. Chem. Soc.* **2014**, *136* (44), 15749−15756.
(31) Hiszpanski, A. M.; Lee, S. S.; Wang, H.; Woll, A. R.; Nuckolls, C.; Loo, Y. L. Post-Deposition Processing Methods to Induce Preferential Orientation in Contorted Hexabenzocoronene Thin Films. *ACS Nano* **2013**, *7* (1), 294−300.
(32) Hiszpanski, A. M.; Loo, Y.-L. Directing the Film Structure of Organic Semiconductors via Post-Deposition Processing for Transistor and Solar Cell Applications. *Energy Environ. Sci.* **2014**, *7*, 592−608.
(33) Lee, S. S.; Kim, C. S.; Gomez, E. D.; Purushothaman, B.; Toney, M. F.; Wang, C.; Hexemer, A.; Anthony, J. E.; Loo, Y.-L. Controlling Nucleation and Crystallization in Solution-Processed Organic Semiconductors for Thin-Film Transistors. *Adv. Mater.* **2009**, *21*, 3605−3609.
(34) Zeidell, A. M.; Tyznik, C.; Jennings, L.; Zhang, C.; Lee, H.; Guthold, M.; Vardeny, Z. V.; Jurchescu, O. D. Enhanced Charge Transport in Hybrid Perovskite Field-Effect Transistors via Microstructure Control. *Adv. Electron. Mater.* **2018**, *4* (12), 1800316.
(35) Zheng, Z. H.; Lan, H. B; Su, Z. H.; Peng, H. X.; Luo, J. T.; Liang, G. X.; Fan, P. Single Source Thermal Evaporation of Two-Dimensional Perovskite Thin Films for Photovoltaic Applications. *Sci. Rep.* **2019**, *9* (1), 17422.
(36) Liu, J.; Leng, J.; Wu, K.; Zhang, J.; Jin, S. Observation of Internal Photoinduced Electron and Hole Separation in Hybrid Two-Dimentional Perovskite Films. *J. Am. Chem. Soc.* **2017**, *139* (4), 1432−1435.
(37) Dahlman, C. J.; Decrescent, R. A.; Venkatesan, N. R.; Kennard, R. M.; Wu, G.; Everest, M. A.; Schuller, J. A.; Chabinyc, M. L. Controlling Solvate Intermediate Growth for Phase-Pure Organic Lead Iodide Ruddlesden-Popper (C4H9NH3)2(CH3NH3)n-1Pb nI3 n+1 Perovskite Thin Films. *Chem. Mater.* **2019**, *31* (15), 5832−5844.
(38) Quintero-Bermudez, R.; Gold-Parker, A.; Proppe, A. H.; Munir, R.; Yang, Z.; Kelley, S. O.; Amassian, A.; Toney, M. F.; Sargent, E. H. Compositional and Orientational Control in Metal Halide Perovskites of Reduced Dimensionality. *Nat. Mater.* **2018**, *17* (10), 900−907.
(39) Zhang, X.; Munir, R.; Xu, Z.; Liu, Y.; Tsai, H.; Nie, W.; Li, J.; Niu, T.; Smilgies, D. M.; Kanatzidis, M. G.; et al. Phase Transition Control for High Performance Ruddlesden−Popper Perovskite Solar Cells. *Adv. Mater.* **2018**, *30* (21), 1707166.
(40) Cheng, P.; Xu, Z.; Li, J.; Liu, Y.; Fan, Y.; Yu, L.; Smilgies, D. M.; Müller, C.; Zhao, K.; Liu, S. F. Highly Efficient Ruddlesden-Popper Halide Perovskite PA 2 MA 4 Pb 5 I 16 Solar Cells. *ACS Energy Lett.* **2018**, *3* (8), 1975−1982.
(41) Sanchez-Botero, L.; Dimov, A. V.; Li, R.; Smilgies, D. M.; Hinestroza, J. P. In Situ and Real-Time Studies, via Synchrotron X-Ray Scattering, of the Orientational Order of Cellulose Nanocrystals during Solution Shearing. *Langmuir* **2018**, *34* (18), 5263−5272.
(42) Zhang, J.; Zhang, L.; Li, X.; Zhu, X.; Yu, J.; Fan, K. Binary Solvent Engineering for High-Performance Two-Dimensional Perovskite Solar Cells. *ACS Sustainable Chem. Eng.* **2019**, *7* (3), 3487−3495.
(43) Lin, Y.; Fang, Y.; Zhao, J.; Shao, Y.; Stuard, S. J.; Nahid, M. M.; Ade, H.; Wang, Q.; Shield, J. E.; Zhou, N.; Moran, A. M.; Huang, J. Unveiling the Operation Mechanism of Layered Perovskite Solar Cells. *Nat. Commun.* **2019**, *10* (1), 1008.
(44) Chen, A. Z.; Shiu, M.; Deng, X.; Mahmoud, M.; Zhang, D.; Foley, B. J.; Lee, S. H.; Giri, G.; Choi, J. J. Understanding the Formation of Vertical Orientation in Two-Dimensional Metal Halide Perovskite Thin Films. *Chem. Mater.* **2019**, *31* (4), 1336−1343.
(45) Chen, A. Z.; Choi, J. J. Crystallographic Orientation and Layer Impurities in Two-Dimensional Metal Halide Perovskite Thin Films. *J. Vac. Sci. Technol., A* **2020**, *38* (1), 010801.
(46) Nie, W.; Tsai, H.; Asadpour, R.; Blancon, J. C.; Neukirch, A. J.; Gupta, G.; Crochet, J. J.; Chhowalla, M.; Tretiak, S.; Alam, M. A.; et al. High-Efficiency Solution-Processed Perovskite Solar Cells with Millimeter-Scale Grains. *Science (Washington, DC, U. S.)* **2015**, *347* (6221), 522−525.
(47) Zeng, Q.; Zhang, X.; Feng, X.; Lu, S.; Chen, Z.; Yong, X.; Redfern, S. A. T.; Wei, H.; Wang, H.; Shen, H.; et al. Polymer-Passivated Inorganic Cesium Lead Mixed-Halide Perovskites for Stable and Efficient Solar Cells with High Open-Circuit Voltage over 1.3 V. *Adv. Mater.* **2018**, *30* (9), 1705393.
(48) Zhao, X.; Tian, L.; Liu, T.; Liu, H.; Wang, S.; Li, X.; Fenwick, O.; Lei, S.; Hu, W. Room-Temperature-Processed Fullerene Single-Crystalline Nanoparticles for High-Performance Flexible Perovskite Photovoltaics. *J. Mater. Chem. A* **2019**, *7* (4), 1509−1518.
(49) Tan, S.; Zhou, N.; Chen, Y.; Li, L.; Liu, G.; Liu, P.; Zhu, C.; Lu, J.; Sun, W.; Chen, Q.; et al. Effect of High Dipole Moment Cation on Layered 2D Organic−Inorganic Halide Perovskite Solar Cells. *Adv. Energy Mater.* **2018**, *9* (5), 1803024.
(50) Qin, P. L.; Yang, G.; Ren, Z. W.; Cheung, S. H.; So, S. K.; Chen, L.; Hao, J.; Hou, J.; Li, G. Stable and Efficient Organo-Metal Halide Hybrid Perovskite Solar Cells via π-Conjugated Lewis Base Polymer Induced Trap Passivation and Charge Extraction. *Adv. Mater.* **2018**, *30* (12), 1706126.
(51) Liang, P. W.; Liao, C. Y.; Chueh, C. C.; Zuo, F.; Williams, S. T.; Xin, X. K.; Lin, J.; Jen, A. K. Y. Additive Enhanced Crystallization of Solution-Processed Perovskite for Highly Efficient Planar-Heterojunction Solar Cells. *Adv. Mater.* **2014**, *26* (22), 3748−3754.
(52) Li, Y.; Zhao, Y.; Chen, Q.; Yang, Y.; Liu, Y.; Hong, Z.; Liu, Z.; Hsieh, Y. T.; Meng, L.; Li, Y.; et al. Multifunctional Fullerene Derivative for Interface Engineering in Perovskite Solar Cells. *J. Am. Chem. Soc.* **2015**, *137* (49), 15540−15547.

https://dx.doi.org/10.1021/acs.nanolett.0c03914
Nano Lett. 2020, 20, 8880−8889

(53) Wang, K.; Wu, C.; Yang, D.; Jiang, Y.; Priya, S. Quasi-Two-Dimensional Halide Perovskite Single Crystal Photodetector. *ACS Nano* **2018**, *12* (5), 4919−4929.
(54) Peng, W.; Yin, J.; Ho, K. T.; Ouellette, O.; De Bastiani, M.; Murali, B.; El Tall, O.; Shen, C.; Miao, X.; Pan, J.; et al. Ultralow Self-Doping in Two-Dimensional Hybrid Perovskite Single Crystals. *Nano Lett.* **2017**, *17* (8), 4759−4767.
(55) Duijnstee, E. A.; Ball, J. M.; Le Corre, V. M.; Koster, L. J. A.; Snaith, H. J.; Lim, J. Toward Understanding Space-Charge Limited Current Measurements on Metal Halide Perovskites. *ACS Energy Lett.* **2020**, *5*, 376−384.
(56) Chen, Y.; Sun, Y.; Peng, J.; Tang, J.; Zheng, K.; Liang, Z. 2D Ruddlesden−Popper Perovskites for Optoelectronics. *Adv. Mater.* **2018**, *30*, 1703487.
(57) Zhao, X.; Zhang, F.; Yi, C.; Bi, D.; Bi, X.; Wei, P.; Luo, J.; Liu, X.; Wang, S.; Li, X.; et al. A Novel One-Step Synthesized and Dopant-Free Hole Transport Material for Efficient and Stable Perovskite Solar Cells. *J. Mater. Chem. A* **2016**, *4* (42), 16330−16334.
(58) Domanski, K.; Correa-Baena, J. P.; Mine, N.; Nazeeruddin, M. K.; Abate, A.; Saliba, M.; Tress, W.; Hagfeldt, A.; Grätzel, M. Not All That Glitters Is Gold: Metal-Migration-Induced Degradation in Perovskite Solar Cells. *ACS Nano* **2016**, *10* (6), 6306−6314.
(59) Wang, Q.; Chen, B.; Liu, Y.; Deng, Y.; Bai, Y.; Dong, Q.; Huang, J. Scaling Behavior of Moisture-Induced Grain Degradation in Polycrystalline Hybrid Perovskite Thin Films. *Energy Environ. Sci.* **2017**, *10* (2), 516−522.
(60) Christians, J. A.; Schulz, P.; Tinkham, J. S.; Schloemer, T. H.; Harvey, S. P.; Tremolet De Villers, B. J.; Sellinger, A.; Berry, J. J.; Luther, J. M. Tailored Interfaces of Unencapsulated Perovskite Solar Cells for > 1,000 h Operational Stability. *Nat. Energy* **2018**, *3* (1), 68−74.
(61) Domanski, K.; Roose, B.; Matsui, T.; Saliba, M.; Turren-Cruz, S. H.; Correa-Baena, J. P.; Carmona, C. R.; Richardson, G.; Foster, J. M.; De Angelis, F.; et al. Migration of Cations Induces Reversible Performance Losses over Day/night Cycling in Perovskite Solar Cells. *Energy Environ. Sci.* **2017**, *10* (2), 604−613.
(62) Zuo, L.; Guo, H.; deQuilettes, D. W.; Jariwala, S.; De Marco, N.; Dong, S.; DeBlock, R.; Ginger, D. S.; Dunn, B.; Wang, M.; Yang, Y. Polymer-Modified Halide Perovskite Films for Efficient and Stable Planar Heterojunction Solar Cells. *Sci. Adv.* **2017**, *3* (8), e1700106.
(63) Shao, Y.; Fang, Y.; Li, T.; Wang, Q.; Dong, Q.; Deng, Y.; Yuan, Y.; Wei, H.; Wang, M.; Gruverman, A.; et al. Grain Boundary Dominated Ion Migration in Polycrystalline Organic-Inorganic Halide Perovskite Films. *Energy Environ. Sci.* **2016**, *9* (5), 1752−1759.
(64) Yuan, Y.; Huang, J. Ion Migration in Organometal Trihalide Perovskite and Its Impact on Photovoltaic Efficiency and Stability. *Acc. Chem. Res.* **2016**, *49* (2), 286−293.

https://dx.doi.org/10.1021/acs.nanolett.0c03914
Nano Lett. 2020, 20, 8880−8889